

Rotordynamic behaviour of a micro-turbine rotor on air bearings: modelling techniques and experimental verification

T. Waumans, P. Vleugels, J. Peirs, F. Al-Bender, D. Reynaerts

Katholieke Universiteit Leuven,

Department of Mechanical Engineering,

Celestijnenlaan 300 B, B-3001, Heverlee, Belgium

e-mail: tobias.waumans@mech.kuleuven.be

Abstract

Current trends in micro-turbomachinery stress the need for adequate rotordynamic models. These models should allow accurate prediction of critical speeds, imbalance response and stable operation range of micro-turbomachinery rotor-bearing systems. This paper gives an overview of the total rotordynamic modelling process of a micro-turbine rotor supported on aerostatic bearings. A both accurate and efficient modelling technique is outlined to obtain static and dynamic air bearing properties. These bearing coefficients serve as input for a rotordynamic model yielding damped natural frequencies, unbalance response and stability limits. Experimental verification confirms a good agreement with the predicted critical speeds.

Nomenclature

A_o	annular curtain area at gap entrance [m ²]
c	journal bearing nominal radial clearance [μm]
c_{ij}	bearing damping coefficient [N s/ μm or Nm s/rad]
C_d	entrance flow coefficient of discharge
f	external force acting on rotor [N]
h	thrust bearing nominal clearance [μm]
H	normalised film height
I_t	rotor transverse moment of inertia [gmm ²]
I_p	rotor polar moment of inertia [gmm ²]
k_{ij}	bearing stiffness coefficient [N/ μm or Nm/rad]
L	journal bearing length [mm]
L_b	distance between journal bearing centres [mm]
L_p	distance between measurement planes [mm]
L_{tot}	total rotor length [mm]
m	rotor mass [g]
\dot{m}	mass flow [g/s]
\dot{m}_o	gap entrance flow [g/s]
p_a	atmospherical pressure [Pa]
p_o	gap entrance pressure [Pa]
p_s	supply pressure [Pa]

p_t	extrapolated pressure at gas entrance [Pa]
P	normalised film pressure
P_f	bearing viscous losses [W]
r	journal bearing radius [mm]
\mathfrak{R}	gas constant [J/kg K]
r_i	thrust bearing inner radius [mm]
r_o	thrust bearing outer radius [mm]
T	external torque acting on rotor [Nm]
T_s	gas temperature at stagnation [K]
V	relative sliding velocity [m/s]
W	bearing load carrying capacity [N]
ϕ_d	rotor disc diameter [mm]
ϕ_{fh}	feedhole diameter [μm]
ϕ_s	rotor shaft diameter [mm]
γ	thrust bearing tilt angle [rad]
ϵ	journal bearing eccentricity ratio e/c
κ	ratio of specific heats
μ	gas viscosity [kg/m s]
ν	perturbation frequency [Hz]
ω	rotor speed [Hz]
ω_{cyl}	cylindrical critical speed [Hz]
ω_{con}	conical critical speed [Hz]

1 Introduction

Recently, a growing interest in micro-turbomachinery applications is noticeable. Miniaturisation in a lot of research domains has led to a demand for small-scale systems running at high operational speeds. In most of the cases air bearings offer low frictional losses, high reliability, long bearing life and high operational temperatures. The cost of all these benefits lies in the sometimes complicated design and optimisation process encountered when using air bearings.

Currently, extensive research is done to develop fuel based micro power generating units based on a gas-turbine cycle. These units are intended to serve as autonomous and portable power supplies with a higher energy density than the best performing batteries. Projects are running at MIT [1], Tohoku University, Tokyo University, ETH Zurich and Katholieke Universiteit Leuven [2].

The research of this paper is situated within the PowerMEMS-project of the Katholieke Universiteit Leuven. The project goal is the development of a micro-gasturbine with an output power ranging from 100 W to 1 kW, while the overall size should not exceed 1 dm³. The target rotational speed is set to 500,000 rpm with a compressor and turbine diameter of 20 mm.

Aerodynamic foil bearings are the most promising choice for meeting the stringent bearing requirements. For prototyping purposes, rigid aerostatic and hybrid bearings will be used. The test-setup described in this paper is a first simplified prototype to validate bearing modelling techniques and balancing methods.

The first section of this paper describes the test-setup components and instrumentation. The rotordynamic modelling process is divided into two steps. First, an extensive overview is given on air bearing modelling techniques. After this, the dynamic behaviour of the rotor-bearing system is examined. Finally, experiments are performed to validate the predicted critical speeds and stability limits.

Other recent rotordynamic studies of rotors supported on air bearings are done by San Andres in [3, 4].

2 Description of micro-turbine test-setup

2.1 General overview

Figure 1 gives an exploded view of the micro-turbine test-setup. The setup was mainly designed to perform balancing experiments on a miniature high-speed rotor.

The rotating part of the setup consists of a shaft with two shrink-fitted rotor discs. These discs are actually dummy representatives of the future turbine and compressor part. The rotor is supported by a split aerostatic bearing. The bearing parts fit into a housing which provides air supply connection and sensor interface. Two covers close the total unit while guaranteeing proper alignment of the split bearing parts.

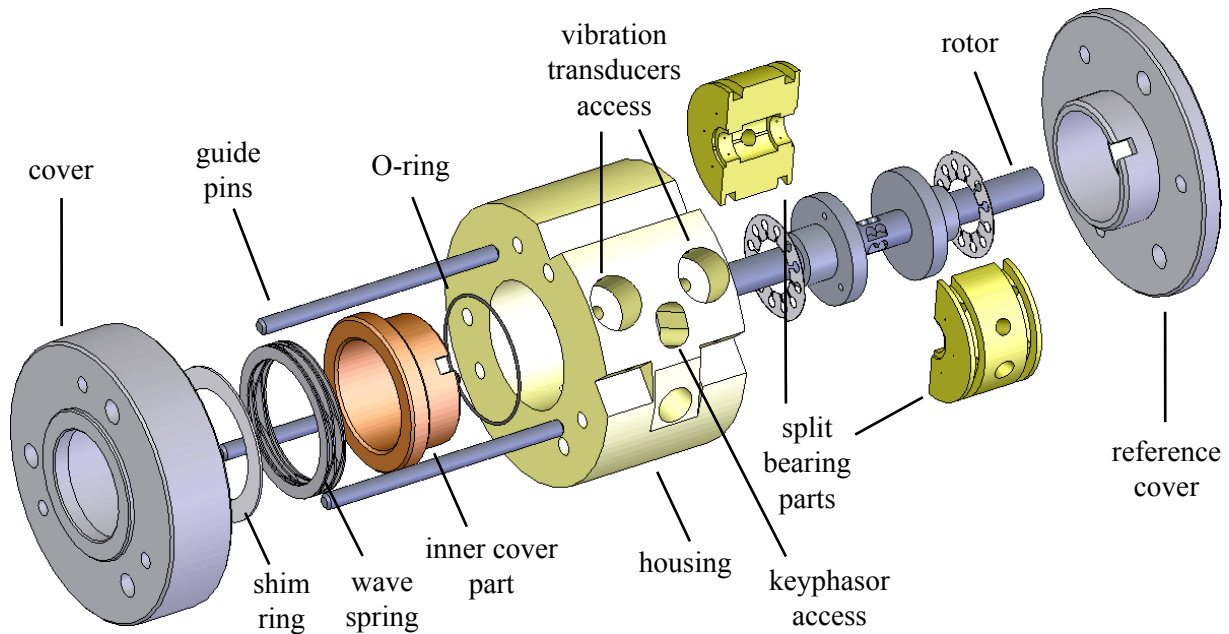


Figure 1: Exploded view of the test-setup.

Accurate fitting and alignment of the two bearing halves proved to be one of the most critical issues of the setup. An alternative of this split bearing approach would be to make one of the rotor discs dismountable. This however does not guarantee the rotor having repetitive imbalance conditions.

The current setup can be disassembled by removing the left outer and inner cover parts, allowing the core unit to be shifted out. The actual alignment of the bearing halves is done by a tight tolerance fit into the inner cylinder of the housing. A wave spring followed by an inner cover part pushes the two halves against a reference cover. This method should allow easy and repetitive mounting of the setup with alignment tolerances within a fraction of the air bearing clearances.

Figure 2 shows a detail view of the core unit consisting of rotor and split bearing parts. In the centre of the rotor shaft, between both rotor discs, a simple Pelton impulse turbine is machined to drive the rotor with pressurised air. A stationary nozzle as well as an exhaust hole are incorporated into each split bearing half. A non-destructive technique of applying small test masses is used for balancing purposes. One or more balancing foils can be mounted on each rotor disc with thicknesses between $40\ \mu\text{m}$ to $200\ \mu\text{m}$, yielding a mass-eccentricity value of $1.56 \times 10^{-5}\ \text{gm}$ to $7.82 \times 10^{-5}\ \text{gm}$ respectively. The foils have a tight tolerance fit on the $\varnothing 10\ \text{mm}$ rotor disc part. Three M1.6 screws fix the foils to the rotor disc with indexing steps of 30° . This technique allows reversible application of virtually any static or dynamic imbalance by choosing the right combination of foil thickness and mutual orientation.

Table 1 summarises the most important rotor parameters.

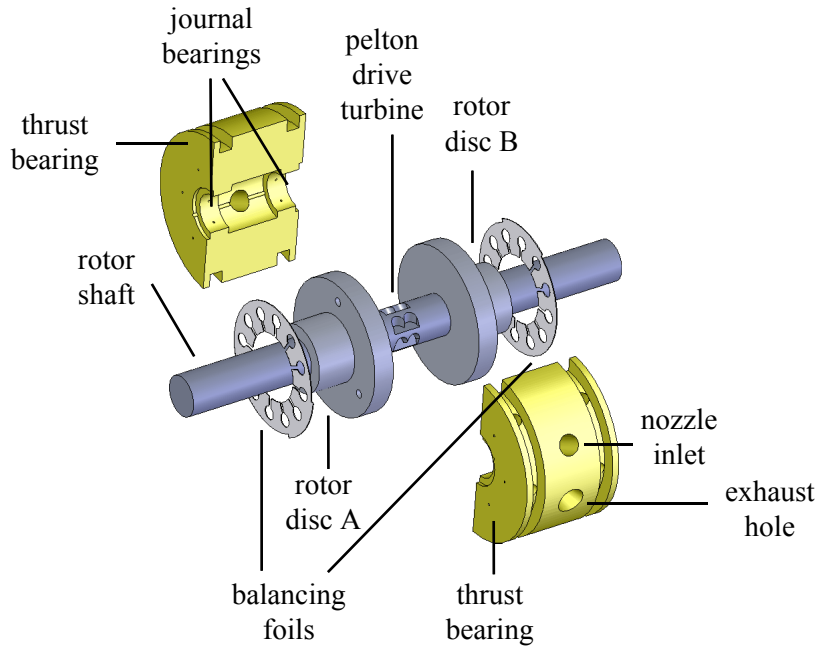


Figure 2: Detail view of the rotor and bearing assembly.

rotor parameters	value
shaft diameter ϕ_s	6 mm
disc diameter ϕ_d	20 mm
total length L_{tot}	65 mm
total mass m	21.3 g
transverse moment of inertia I_t	5842 gmm ²
polar moment of inertia I_p	349 gmm ²
distance between journal bearing centres L_b	11 mm
distance between measurement planes L_p	18 mm
first bending mode	5.186 kHz

Table 1: Rotor parameters of the test rotor.

2.2 Instrumentation

According to theory [5], the number of balancing and measurement planes should be at least equal to the number of critical speeds traversed. The maximum attainable speed of 102.000 rpm (1.7 kHz) lies far below the first bending mode of the rotor (5.186 kHz). Two measurement planes are therefore sufficient for the current test-setup and operational speed range.

Two fiber optical vibration transducers are installed to measure the distance between each rotor disc and the stationary housing. The transducers measure the amount of light reflected by the target surface. For small displacements ($\pm 50 \mu\text{m}$) there exists a nearly linear relationship between the amount of reflected light and target distance. An in-house developed electronic circuit provides an analog voltage signal that is read in by the data acquisition system.

Phase information about the rotor vibration can only be obtained if the recorded signals are triggered to a keyphasor signal. This reference signal tracks a fixed mark on the rotor shaft and results each revolution in a single trigger pulse. A Mechanical Technology Incorporated KD310 optical sensor is used for recording this mark.

Figure 3 summarises the signal path and measurement conventions. The vibrational data of both rotor discs

and the keyphasor signal are sent to an oscilloscope and an National Instruments PXI-6123 data acquisition system. The data is read into the computer and a MATLAB program performs the actual analysis. The trigger signal acts as a reference to make all measured signals perfectly periodical. On this periodical data a frequency analysis is carried out to provide rotor speed and complex vibrational spectra of both rotor discs. Both steady-state and transient measurements can be performed.

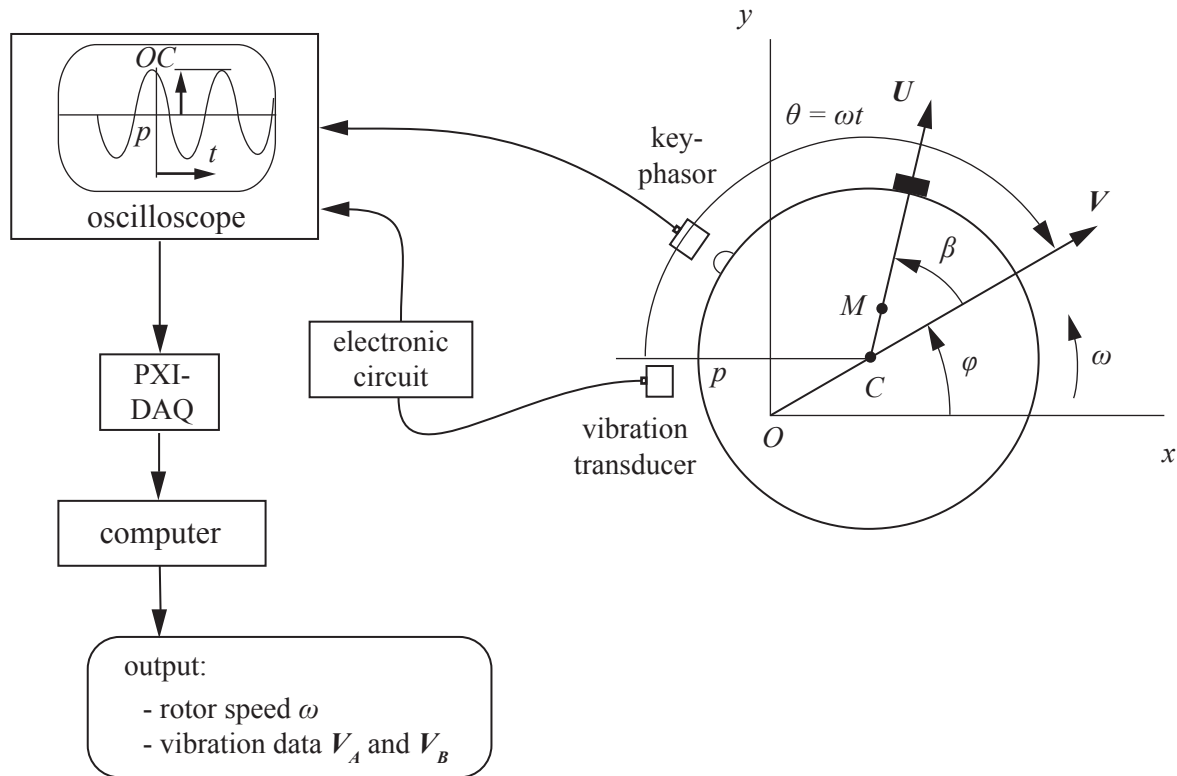


Figure 3: Overview of the measurement conventions and signal processing. O represents the bearing geometrical centre, C the rotor geometrical centre and M the rotor mass centre. At rotor speed ω the imbalance force U results in the imbalance response V with phase angle θ .

2.3 Air bearing geometry

As discussed in the introduction, first turbine prototypes and setups will work with non-conformable (rigid) aerostatic bearings. The split bearing of this setup was designed for stable operation up to 300.000 rpm at 6 bar (absolute) supply pressure.

The exploded view of figure 2 reveals the journal bearing surfaces. The radius r of the plain journal bearing is 3 mm with a length L of 3 mm yielding a length-to-diameter ratio of 0.5. The bearing is fed with six inherent restriction feedholes placed on the bearing centerline. Table 2 summarises the geometrical properties of the journal bearings. Due to manufacturing tolerances, the actual values always differ slightly from the original design value. The actual radial clearance is measured both with a precision internal micrometer and a Renishaw OMP40 touch probe on a KERN MMP micro-milling machine. The feedholes are produced by micro-EDM and are afterwards inspected with a WYKO NT3300 optical profiler.

Two aerostatic thrust bearings support the rotor axially. The inner radius r_i is 4 mm and the outer radius r_o equals 10 mm. Six inherent restriction feedholes are placed at $r = 7$ mm. As for the journal bearings, the actual geometrical properties are inspected after machining. Table 3 lists the design value and the actual value of the different thrust bearing properties.

journal bearing	design value	actual value
radius r	3 mm	-
nominal radial clearance c	7.5 μm	11 μm
length L	3 mm	3 \pm 0.1 mm
feedhole type	inherent restrictor	-
feedhole arrangement	6 centrally placed feedholes	-
feedhole diameter ϕ_{fh}	300 μm	325 μm

Table 2: Geometrical properties of the journal bearing.

Due to the large thrust bearing surface compared to the total rotor length, there exists a considerable tilt effect of the thrust bearings in case of conical rotor vibration. This should certainly be taken into account when calculating the critical speeds and imbalance response.

thrust bearing	design value	actual value
inner radius r_i	4 mm	4 \pm 0.1 mm
outer radius r_o	10 mm	10 \pm 0.1 mm
nominal clearance h	10 μm	15 μm
feedhole type	inherent restrictor	-
feedhole arrangement	6 feedholes placed at $r = 7$ mm	-
feedhole diameter ϕ_{fh}	300 μm	375 μm

Table 3: Geometrical properties of the thrust bearing.

3 Air bearing modelling techniques

Bearing support characteristics form the main input for the calculation of every aspect of the rotordynamic behaviour. Further on, an overview will be given about the applied modelling and simulation techniques for the aerostatic bearings. The final output of these calculations are the bearing characteristics for different operational parameters.

3.1 Governing equations

The viscous gas film flow between the stationary housing surface and rotating shaft is modelled by the compressible Reynolds equation [6]. This equation yields the pressure distribution between two surfaces as a function of the relative shearing velocity.

$$\nabla \cdot \left[\frac{p_a c^2}{12\mu} PH^3 \nabla P - \frac{1}{2} PH \mathbf{V} \right] = \frac{\partial}{\partial t} (PH) \quad (1)$$

wherein pressure P and height H are normalised with respect to atmospheric pressure p_a and radial clearance c respectively. μ stands for the gas viscosity, while \mathbf{V} indicates the relative sliding velocity between the bearing surfaces. Three contributions can be distinguished: a Poiseuille pressure induced flow term, a Couette velocity induced term and a squeeze term.

For certain geometrical bearing configuration and working parameters, the above stated equation is solved by using a finite difference calculation scheme. Essential to this process are suitable boundary conditions. At the bearing outer surfaces, the pressure P should always remain one ($p = p_a$). At feedholes however, the boundary conditions are less obvious. A correct and practical usable entrance flow model is hereby indispensable.

3.2 Entrance flow model

The flow path from feedhole to atmospheric pressure can be divided into three different flow regions (figure 4). First the flow accelerates in the feedhole itself reaching maximum speed somewhere at the gap entrance. This region is called the feed region. Then, the flow begins to decelerate due to viscous friction and the diffuser effect. Fluid inertia forces gradually become less important. This second region is termed the entrance region. Finally, viscous forces are dominant up to the exit. This last region is named the viscous region and normally fills the greatest part of the bearing surface.

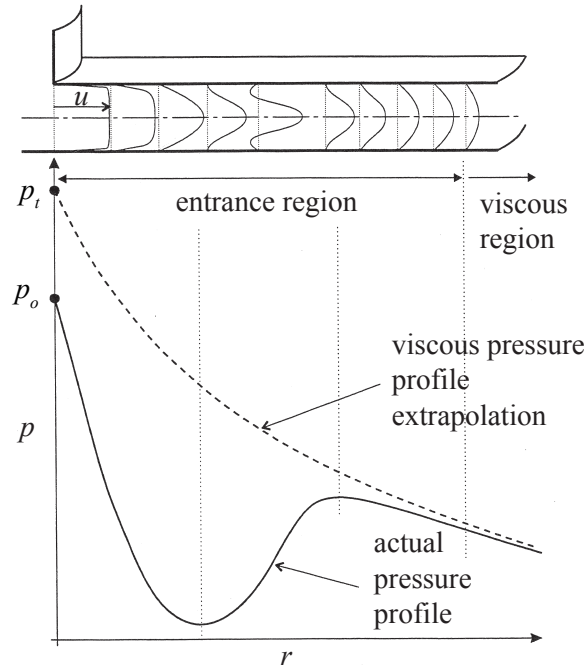


Figure 4: Entrance flow region.

For the first flow region, the Euler equation can be used to relate mass flow through the feedhole to pressure drop (from supply pressure p_s to the gap entrance pressure p_o). From the start of viscous flow up to atmospheric pressure p_a , one can rely on the above stated Reynolds equation. For the description of flow in the intermediate entrance region several models and theories have been developed in the past. Most known are the empirical orifice formulas and Vohr's correlation formula.

However, the boundary-layer equations describing this entrance flow can be analytically solved by separating the velocity into an amplitude and a profile function [7]. This method allows the calculation of the actual pressure profile from gap entrance to atmospheric pressure.

It would make bearing calculation more practical if one could formulate a lumped-parameter formula to quantify the entrance effects without having to solve the actual pressure profile for each given bearing configuration. The following equation relates the mass flow to the pressure ratio p_t/p_s , in which p_t stands for the theoretical pressure at gap entrance if the viscous profile would be extrapolated.

$$\dot{m}_o = C_d A_o \sqrt{\frac{2\kappa}{\kappa - 1}} \frac{p_s}{\sqrt{\Re T_s}} \phi_e \left(\frac{p_t}{p_s} \right) \quad (2)$$

In this equation A_o represents the annular curtain area at gap entrance, κ is the ratio of specific heats of the gas, \Re the gas constant, T_s the gas temperature at stagnation and ϕ_e represents the nozzle function.

The values of the coefficient of discharge C_d are obtained out of solution data of the actual pressure profile for different entrance parameters. C_d is tabulated as a function of bearing geometry, gas properties and p_t/p_s .

In practice, the below iteration process should be followed to determine the appropriate boundary value p_t at each feedhole.

1. Choose a starting value for p_t . This value serves as a boundary condition for calculating the viscous pressure profile over the whole bearing area.
2. The obtained pressure profile allows to determine the film flow.
3. From the lumped-parameter entrance model, the entrance flow can be calculated.
4. Both flow quantities should match. If not, adjust p_t by using for instance the Newton-Raphson technique.

3.3 Bearing characteristics

A given bearing geometry in combination with its working parameters forms the input for calculating the bearing characteristics. During steady-state operation, one is for example interested in static bearing characteristics as load carrying capacity and frictional losses. More important for rotordynamic study, are dynamic characteristics as stiffness and damping properties.

3.3.1 Static characteristics

Figure 5 shows the static pressure profile of the journal bearing with geometrical parameters as in table 2 at a rotational speed ω of 100.000 rpm and eccentricity ϵ of 0.025. At these working conditions, the rotor weight is compensated by the load carrying capacity of both journal bearings. Table 4 lists the journal bearing characteristics.

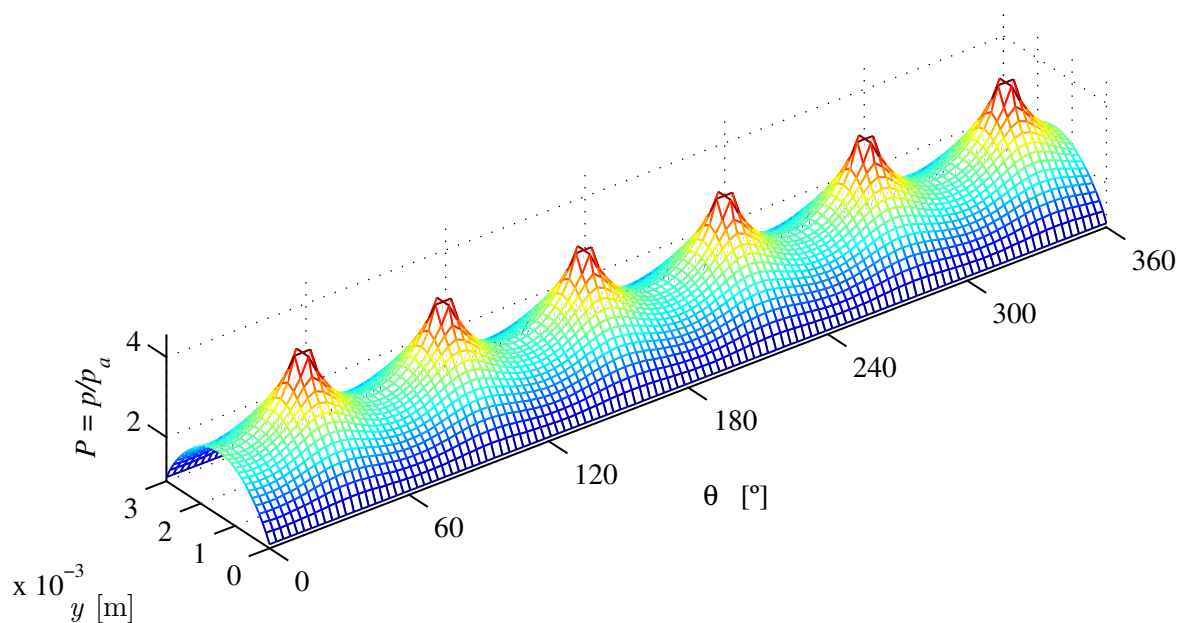
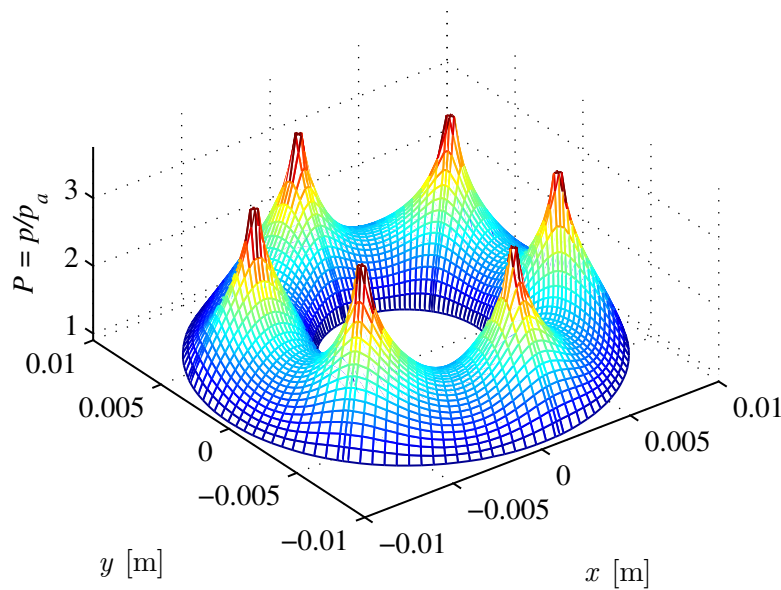


Figure 5: Static pressure profile of the journal bearings at a rotational speed ω of 100.000 rpm and eccentricity ϵ of 0.025.

For the same working conditions, the pressure profile of the thrust bearing is calculated and plotted in figure 6. Its characteristics are given in table 5.

journal bearing	value
rotational speed ω	100.000 rpm
eccentricity ϵ	0.025
supply pressure p_s	6 bar (absolute)
load carrying capacity W	0.094 N
viscous losses P_f	0.085 W
total mass flow \dot{m}	0.084 g/s
synchronous stiffness \mathbf{k} [N/ μm]	$\begin{bmatrix} 0.340 & 0.005 \\ -0.005 & 0.340 \end{bmatrix}$
synchronous damping \mathbf{c} [N s/m]	$\begin{bmatrix} 0.721 & -0.031 \\ 0.031 & 0.724 \end{bmatrix}$

Table 4: Static and dynamic characteristics of the journal bearing.

Figure 6: Static pressure profile of the thrust bearings at a rotational speed ω of 100.000 rpm and zero tilt angle γ .

3.3.2 Stiffness and damping coefficients

When interested in a system's critical speeds, imbalance response and stability limit, the dynamic bearing properties must first be determined. For the journal bearing of figure 7 the spring and damper forces are formulated as:

$$\begin{Bmatrix} f_x \\ f_y \end{Bmatrix} = \begin{bmatrix} k_{xx} & k_{xy} \\ k_{yx} & k_{yy} \end{bmatrix} \cdot \begin{Bmatrix} x \\ y \end{Bmatrix} + \begin{bmatrix} c_{xx} & c_{xy} \\ c_{yx} & c_{yy} \end{bmatrix} \cdot \begin{Bmatrix} \dot{x} \\ \dot{y} \end{Bmatrix} \quad (3)$$

where \mathbf{k} and \mathbf{c} are the stiffness and damping-coefficient matrix respectively. A peculiarity about air bearings - and hydrodynamic bearings and seals in general - is the presence of cross-coupled or indirect stiffness and damping terms. These terms are responsible for a reaction force perpendicular to the disturbance. In this way, k_{xy} represents the stiffness coefficient relating displacement in the x -direction due to a force acting in the y -direction. c_{xy} represents the damping coefficient relating velocity in the x -direction due to a force acting in the y -direction.

To describe the dynamical properties of a bearing one needs at least four stiffness and four damping terms.

thrust bearing	value
rotational speed ω	100.000 rpm
tilt angle γ	0 rad
supply pressure p_s	6 bar (absolute)
load carrying capacity W	20.15 N
viscous losses P_f	1.87 W
total mass flow \dot{m}	0.132 g/s
synchronous tilt stiffness k [Nm/rad]	$\begin{bmatrix} 49.491 & -2.129 \\ 2.128 & 49.491 \end{bmatrix}$
synchronous tilt damping c [Nm s/rad]	$\begin{bmatrix} 0.324 & 0.039 \\ -0.039 & 0.324 \end{bmatrix} \times 10^{-3}$

Table 5: Static and dynamic characteristics of the thrust bearing.

Another complication lies in the dependence of these coefficients on the eccentricity ϵ , rotational speed ω and perturbation frequency ν . Assuming a more or less constant steady-state bearing eccentricity, tabulated values of all of these coefficients for different values of rotor speed ω and perturbation frequency ν are necessary in order to predict the rotordynamic behaviour with reasonable accuracy.

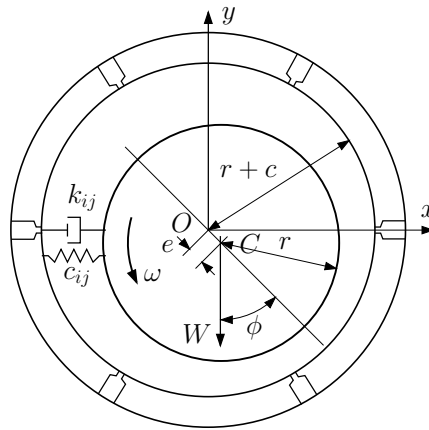


Figure 7: Journal bearing model.

A similar situation exists for the tilt stiffness and damping properties of a thrust bearing. The x and y -direction are replaced by two orthogonal rotational degrees of freedom α and β and forces become torques. The spring and damper torques are given by:

$$\begin{Bmatrix} T_\alpha \\ T_\beta \end{Bmatrix} = \begin{bmatrix} k_{\alpha\alpha} & k_{\alpha\beta} \\ k_{\beta\alpha} & k_{\beta\beta} \end{bmatrix} \cdot \begin{Bmatrix} \alpha \\ \beta \end{Bmatrix} + \begin{bmatrix} c_{\alpha\alpha} & c_{\alpha\beta} \\ c_{\beta\alpha} & c_{\beta\beta} \end{bmatrix} \cdot \begin{Bmatrix} \dot{\alpha} \\ \dot{\beta} \end{Bmatrix} \quad (4)$$

The most common way of calculating air bearing stiffness and damping properties, is by applying a perturbation with frequency ν on the steady-state height profile. This results in a perturbed pressure profile yielding the stiffness and damping forces by integration over the complete bearing surface [6]. These dynamic properties depend on the steady-state working condition, rotational speed ω and perturbation frequency ν . By this method obtained coefficients are in theory only valid for infinitesimally small perturbations. In practice, they prove to be fairly correct when the perturbation reaches up to 40 % of the bearing clearance [9].

Other methods rely on a time-marching ADI-solution (alternating direction implicit) of the Reynolds equation [8].

As an example, figure 8 shows the tilt stiffness and tilt damping coefficients of the thrust bearing of table 3 for rotational frequencies up to 10 kHz (600.000 rpm) and perturbation frequencies up to twice the running

speed. The figure indicates that the dynamic stiffness reaches an asymptotic value at high perturbation frequencies, while the damping tends to zero.

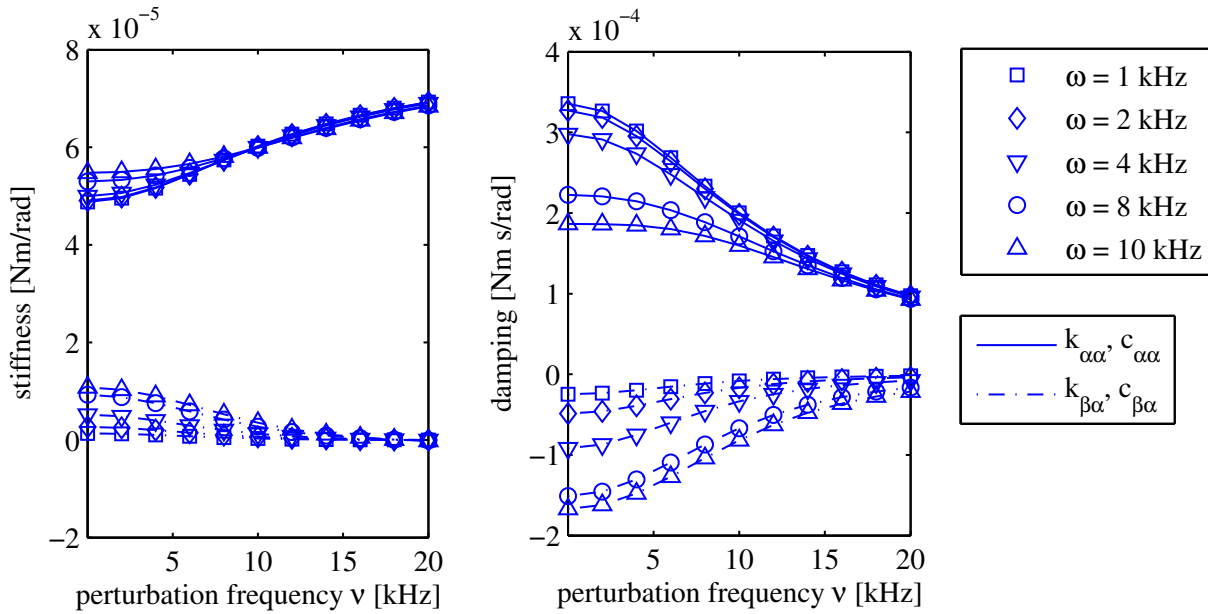


Figure 8: Dynamic tilt properties of the thrust bearing of table 3 for rotational frequencies up to 10 kHz (600.000 rpm) and perturbation frequencies up to twice the running speed.

4 Rotordynamic analysis

The rotordynamic analysis starts by writing down the equations of motion of the rotor using an inertial x, y, z system (figure 9). The rotor is assumed to stay rigid in the speed range of interest. Four degrees of freedom are taken into account, two translational (x and y) and two rotational (α and β). The rotation around the nominal axis of rotation (z) as well as the translational degree of freedom in that direction are omitted. The gyroscopic effect is included in the analysis.

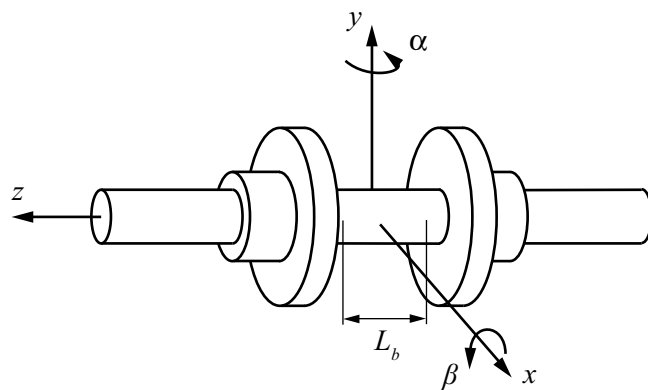


Figure 9: Dynamical model of the rotor.

$$m\ddot{x} + 2c_{xx}\dot{x} + 2k_{xx}x + 2c_{xy}\dot{y} + 2k_{xy}y = f_x \quad (5)$$

$$m\ddot{y} + 2c_{yy}\dot{y} + 2k_{yy}y + 2c_{yx}\dot{x} + 2k_{yx}x = f_y \quad (6)$$

$$I_t\ddot{\alpha} - I_p\omega\dot{\beta} + 2c_{\alpha\alpha}\dot{\alpha} + 2k_{\alpha\alpha}\alpha + 2c_{\beta\alpha}\dot{\alpha} + 2k_{\beta\alpha}\alpha + \frac{1}{2}c_{xx}L_b^2\dot{\alpha} + \frac{1}{2}k_{xx}L_b^2\alpha + \frac{1}{2}c_{xy}L_b^2\dot{\beta} + \frac{1}{2}k_{xy}L_b^2\beta = T_\alpha \quad (7)$$

$$I_t\ddot{\beta} + I_p\omega\dot{\alpha} + 2c_{\beta\beta}\dot{\beta} + 2k_{\beta\beta}\beta + 2c_{\alpha\beta}\dot{\beta} + 2k_{\alpha\beta}\beta + \frac{1}{2}c_{yy}L_b^2\dot{\beta} + \frac{1}{2}k_{yy}L_b^2\beta + \frac{1}{2}c_{yx}L_b^2\dot{\alpha} + \frac{1}{2}k_{yx}L_b^2\alpha = T_\beta \quad (8)$$

The right part of these equations stands for the external forces or couples acting on the rotor. L_b represents the distance between the journal bearing centres.

The first two equations (equation 5 and 6) describe the cylindrical whirling motion of the rotor, while the last two (equation 7 and 8) represent the conical whirling motion. The total system of equations can be decoupled into two independent systems of each two degrees of freedom.

4.1 Damped natural frequencies

An eigenvalue analysis of the homogeneous systems of equations 5 to 8 reveals the damped natural frequencies of the rotor-bearing system. The dependence of the bearing coefficients on both rotor speed ω and perturbation frequency ν makes the solution process iterative. At each rotor speed ω^* , the below outlined calculation scheme should be followed. During the iteration, the bearing properties are obtained out of tabulated values.

1. Calculate the eigenvalues for $\omega = \omega^*$ and $\nu = \nu_1$ (initial guess). This gives a vector of eigenvalues $\lambda_{1'} = \eta_{1'} + j\nu_{1'}$.
2. Seek the zero of $\Delta_\nu(\nu) = \nu_1 - \nu_{1'}$ with an appropriate solving algorithm (for instance Newton-Raphson).
3. When after N steps $\Delta_\nu \simeq 0$, the eigenvalue $\lambda_{N'} = \eta_{N'} + j\nu_{N'}$ describes the damped solution of the system.

An eigenvalue consists of a real part and an imaginary part. The first part η indicates the stability of the solution. According to the Routh-Hurwitz criterium, $\eta < 0$ suggests a stable solution of the system. At $\eta = 0$ the system is marginally stable. This point is called the stability limit. The second imaginary part of the eigenvalue ν represents the natural frequency of the solution.

In figure 10 the outlined process is applied to the rotor-bearing system of the test-setup for speeds up to 2.5 kHz (150.000 rpm) at a supply pressure p_s of 6 bar (absolute). At each speed ω , four eigenvalues are found representing two cylindrical modes and two conical modes, of which one is a forward whirling mode and the other a backward whirling mode. In most cases only the forward whirling modes are excited by rotor imbalance [5].

4.2 Forced synchronous response

Equations 5 to 8 can be reformulated to a matrix equation as follows:

$$m\ddot{x} + c\dot{x} + kx = f \quad (9)$$

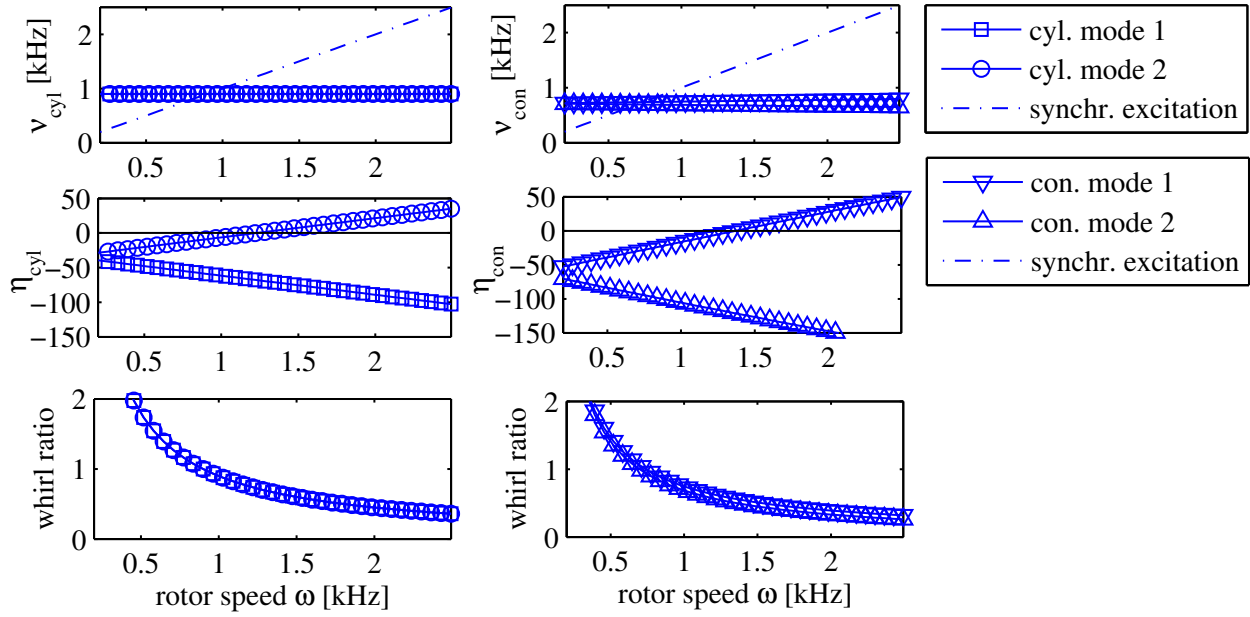


Figure 10: Damped natural frequencies of the test-setup for different values of the rotor speed ω . The upper graphs show the natural frequency ν of both whirling modes, the middle graphs indicate the stability of the solution. The lower plots show the whirl ratio (being ν/ω) of the solution.

wherein m represents the mass matrix, c the damping matrix and k the stiffness matrix of the system. The vector f forms the external force input of the system. The transfer function $H(s)$ which relates force input $F(s)$ to displacement output $X(s)$ is obtained by applying the Laplace transform.

$$s^2mX(s) + scX(s) + kX(s) = F(s) \tag{10}$$

$$H(s) = \frac{X(s)}{F(s)} = \frac{1}{s^2m + sc + k} \tag{11}$$

The synchronous imbalance response can be predicted by evaluating equation 11 at different rotor speeds ω . The iterative procedure explained above can be omitted due to the forced nature of the vibration, meaning $\nu = \omega$. The force input $F(s)$ is generally a combination of a static and dynamic imbalance condition and is proportional to the square of the rotor speed.

5 Experimental results

This section gives an overview of validation experiments conducted on the test-setup. Before performing actual validation experiments of critical speeds and stability limits, the rotor should be sufficiently balanced to safely pass the first two rigid body modes. Hereafter, runup and coastdown experiments were performed to reveal the critical speeds at different supply pressures. At low supply pressures, severe subsynchronous whirling is observed. The results obtained out of these measurements are compared with predicted values.

5.1 Balancing experiments

As explained, the rotor can be considered rigid within the speed range of the experiments (maximum rotor speed $\omega = 1.7$ kHz or 102.000 rpm). Two plane balancing is therefore sufficient. The conventional but

effective method using two balancing planes and influence coefficients is applied [5].

The balancing speed was set to 570 Hz (34.200 rpm) at a bearing supply pressure p_s of 6 bar (absolute). At this rotor speed the amplitude of the rotor vibrations is nearly half the journal bearing clearance ($c = 11 \mu\text{m}$). Table 6 lists the measured synchronous rotor vibrations before balancing, after applying the trial masses on rotor disc A and B and finally after mounting the calculated correction masses. With the stated correction masses the attainment of supercritical speeds up to 102.000 rpm was possible. In most experiments, the available power of the drive turbine prevented reaching even higher rotational speeds.

	speed ω [Hz]	balancing mass	response disc A	response disc B
before balancing	586	-	$4.1 \mu\text{m} \angle 17.1^\circ$	$4.1 \mu\text{m} \angle 152.4^\circ$
trial mass on disc A	569	$5.87 \times 10^{-5} \text{ gm} \angle -135^\circ$	$8.1 \mu\text{m} \angle -93.3^\circ$	$4.2 \mu\text{m} \angle 166.3^\circ$
trial mass on disc B	569	$5.87 \times 10^{-5} \text{ gm} \angle -45^\circ$	$5.0 \mu\text{m} \angle 8.1^\circ$	$0.7 \mu\text{m} \angle -162.3^\circ$
with correction masses	587	A $3.13 \times 10^{-5} \text{ gm} \angle 165^\circ$	$2.0 \mu\text{m} \angle -27.5^\circ$	$0.9 \mu\text{m} \angle -94.7^\circ$
		B $3.13 \times 10^{-5} \text{ gm} \angle -15^\circ$ + $4.70 \times 10^{-5} \text{ gm} \angle -45^\circ$		
	1100		$3.4 \mu\text{m} \angle -85.0^\circ$	$1.6 \mu\text{m} \angle 165.0^\circ$

Table 6: Overview of the results obtained after different balancing steps. The measured response at $\omega = 1100$ Hz (66,000 rpm) indicates the residual rotor imbalance at supercritical speed.

5.2 Runup/coastdown measurements

At different bearing supply pressures the rotor is accelerated to top speed. Then, the supply to the drive turbine is closed, allowing the rotor to slow down. During this coastdown process, the rotor passes through a conical and cylindrical critical speed resulting in increased synchronous rotor vibrations.

Figure 11 shows a waterfall plot of the measured rotor response during a coastdown at a bearing supply pressure p_s of 6 bar (absolute). Figure 12 displays the synchronous component (1X) of this coastdown measurement.

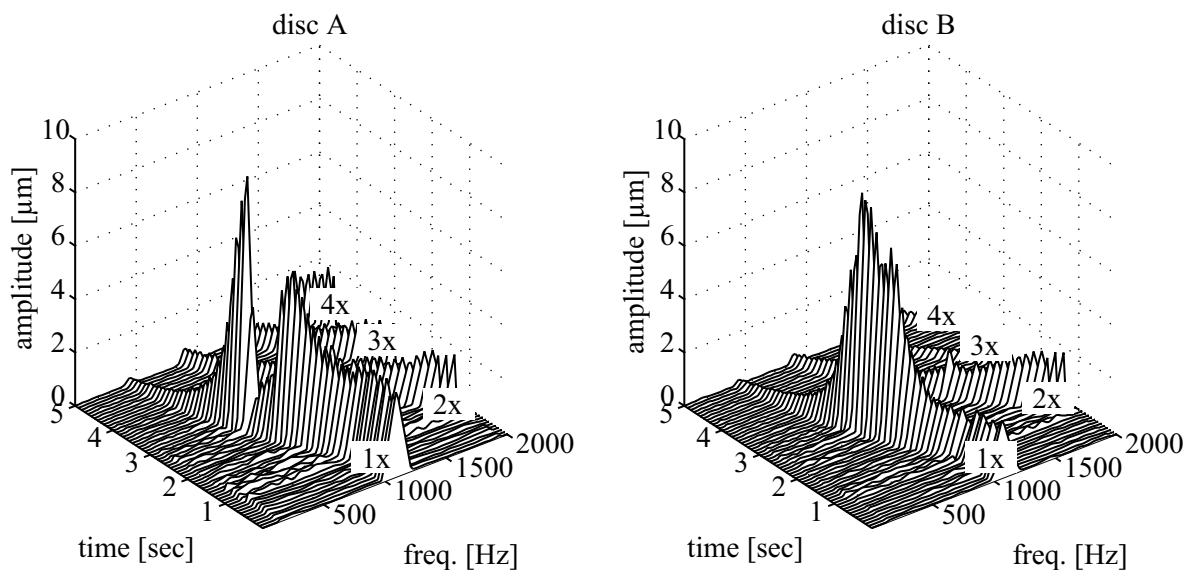


Figure 11: Waterfall plot of the measured rotor response during a coastdown at a bearing supply pressure p_s of 6 bar (absolute). The plot shows the synchronous response (1X) and higher order harmonics (2X, 3X and 4X).

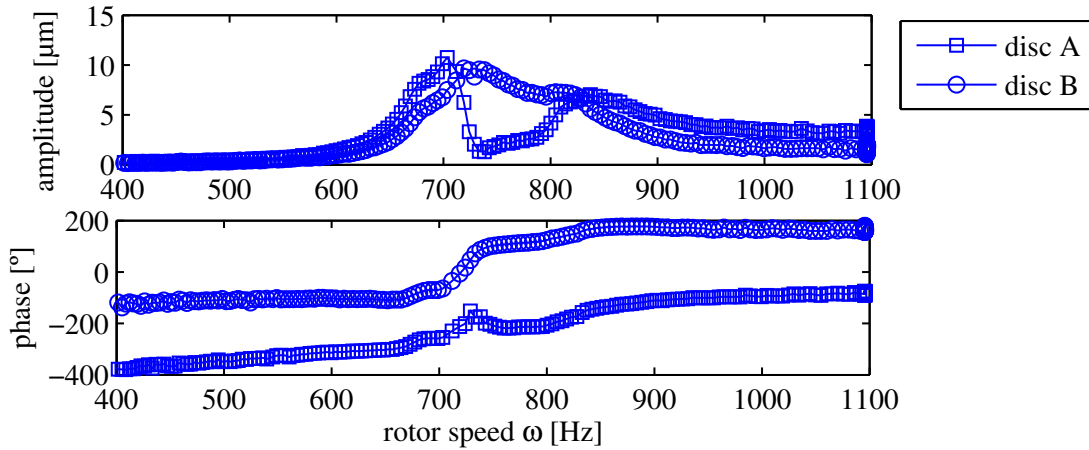


Figure 12: Synchronous rotor response during a coastdown at a bearing supply pressure p_s of 6 bar (absolute).

5.3 Comparison with predictions

5.3.1 Critical speeds

Coastdown measurement were used to identify the cylindrical and conical critical speed at different bearing supply pressures. In order to determine the critical speed of each mode more accurately, the vibration transducer information (z_A and z_B) is separated into $z_{cyl} = (z_A + z_B)/2$ which reveals the presence of cylindrical rotor motion and $z_{con} = (z_A - z_B)/2$ which reveals the occurrence of conical motion. In this way a clear identification is possible, even in the case of closely-spaced critical speeds.

Table 7 lists the experimentally identified and predicted critical speeds for bearing supply pressures p_s from 2 bar up to 8 bar (absolute). The relative difference is also provided. Figure 7 shows the same information in a graph.

supply pressure p_s [bar]	experiment [Hz]	predicted [Hz]	difference [%]
cylindrical crit. speed ω_{cyl}			
2	255	305	19.6
3	410	510	24.4
4	600	690	15
5	730	820	12.3
6	820	900	9.8
7	910	960	5.5
8	990	1007	1.7
conical crit. speed ω_{con}			
2	265	305	15
3	425	450	5.9
4	545	570	4.5
5	635	645	1.6
6	710	700	1.4
7	765	740	3.3
8	820	770	6.1

Table 7: Overview of the experimentally identified and predicted critical speeds.

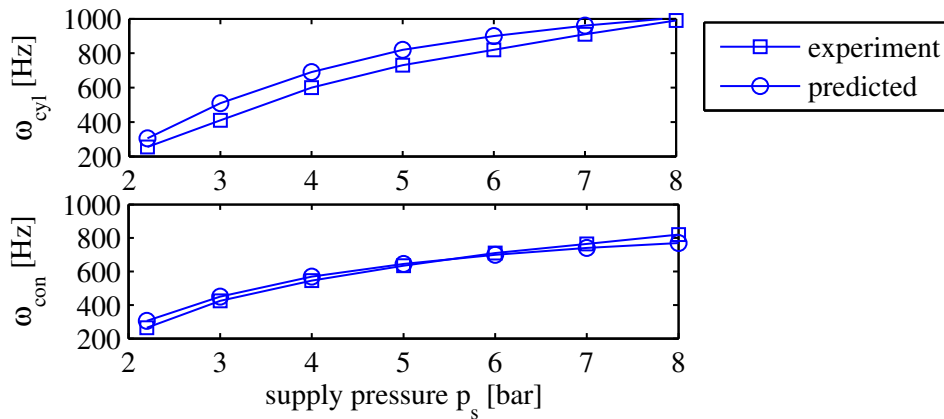


Figure 13: Graphical representation of the experimentally identified and predicted critical speeds.

5.3.2 Stability limit

At low bearing supply pressures and high rotational speeds, severe subsynchronous whirling is observed (figure 14). This whirling is a self-excited phenomenon and is destructive in nature. The point at which the self-excited vibration sets in, is called the stability limit of the rotor-bearing system.

Of all types of air bearings, plain aerodynamic bearings are most prone to subsynchronous whirling which is termed half speed whirling because the whirling occurs at nearly half the rotational speed. Other air bearing types also suffer from this whirling, although at higher rotational speeds. The frequency of the whirling motion is generally not at half the rotational speed, but at a fraction of it (fractional speed whirling). The occurrence of subsynchronous whirling is strongly related to the presence of cross-coupled bearing stiffness and damping coefficients [10].

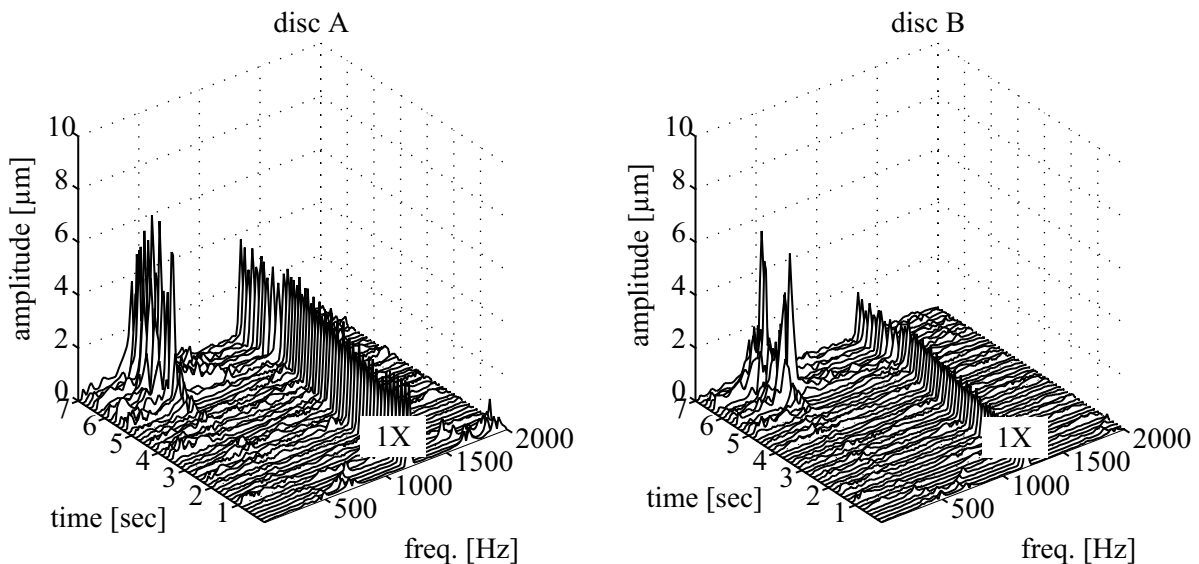


Figure 14: Subsynchronous whirling observed at a bearing pressure p_s of 3 bar (absolute). The rotational speed at which the phenomenon sets in, is 1330 Hz (79800 rpm).

Calculation of the damped natural frequencies allows to predict the stability limit of a given rotor-bearing system. Similar results as shown in figure 10 for a bearing pressure p_s of 3 bar (absolute) yield an estimated stability limit of only 800 Hz. This mismatch can be due to unmodelled external damping between the bearing housing and ground plate.

6 Conclusion and discussion

The total rotordynamic modelling process for a micro-turbine rotor supported on air bearings is outlined. A good agreement is obtained between the predicted critical speeds and the ones identified out of coastdown measurements. This can be seen as a validation of every single step of the rotordynamic modelling effort. Still existing differences between experiments and predictions are possibly due to uncertainties on bearing and rotor properties, roundness and alignment imperfections of the split bearing design and the limited validity of the obtained dynamic bearing properties.

Acknowledgements

This research is sponsored by the IWT, the Institute for the Promotion of Innovation by Science and Technology - Flanders, Belgium; project SBO 030288 "PowerMEMS". T. Waumans is a research assistant of the Fund for Scientific Research (FWO) - Flanders, Belgium. Thanks to M. Ohno and T. Keida for their experimental work.

References

- [1] A. H. Epstein, *Millimeter-scale, micro-electro-mechanical systems gas turbine engines*, ASME Journal of Engineering for Gas Turbines and Power, Vol. 126, 2004, pp. 205-226.
- [2] *Micro power generation based on micro gas turbines: a challenge*, mstnews, No. 4/05, August 2005, pp. 37-39.
- [3] L. San Andres, X. Zhu, *Rotordynamic performance of flexure pivot hydrostatic gas bearings for oil-free turbomachinery*, Proc. of ASME Turbo Expo, June 2004, Vienna, Austria.
- [4] L. San Andres, D. Rubio, T. H. Kim, *Rotordynamic performance of a rotor supported on bump type foil gas bearings: experiments and predictions*, Proc. of ASME Turbo Expo, May 2006, Barcelona, Spain.
- [5] J. M. Vance, *Rotordynamics of turbomachinery*, Wiley-Interscience (1987).
- [6] W. A. Gross, *Gas film lubrication*, John Wiley & Sons Inc. (1962).
- [7] F. Al-Bender, H. Van Brussel, *A method of "separation of variables" for the solution of laminar boundary-layer equations of narrow channel flows*, ASME Journal of Tribology, Vol. 114, July 1992, pp. 630-636.
- [8] K. Czolczynski, *How to obtain stiffness and damping coefficients of gas bearings*, Wear, Vol. 201, 1996, pp. 265-275.
- [9] J. W. Lund, *Review of the concept of dynamic coefficients for fluid film journal bearings*, Journal of Tribology, Vol. 109, January 1987, pp. 37-41.
- [10] J. W. Lund, *The stability of an elastic rotor in journal bearings with flexible, damped supports*, Journal of Applied Mechanics, Trans. ASME, Series E. 1965, Vol. 87(4), pp. 911-920.

